

Doping-induced topological transition and enhancement of thermopower in the Dirac-semimetal system $\text{Cd}_{3-x}\text{Zn}_x\text{As}_2$

J. Fujioka,^{1,*} M. Kriener,^{2,†} D. Hashizume,² Y. Yamasaki,³ Y. Taguchi,² and Y. Tokura^{2,4,5}

¹*Division of Materials Science, University of Tsukuba,
1-1-1 Tennodai, Tsukuba, Ibaraki 305-8573, Japan*

²*RIKEN Center for Emergent Matter Science (CEMS), Wako 351-0198, Japan*

³*National Institute of Material Science, Tsukuba, Ibaraki, 305-0047, Japan*

⁴*Department of Applied Physics and Quantum-Phase Electronics Center (QPEC),
University of Tokyo, Tokyo 113-8656, Japan*

⁵*Tokyo College, University of Tokyo, Hongo, Tokyo 113-8656, Japan*

(Dated: March 19, 2022)

Abstract

Cd_3As_2 is one of the prototypical topological Dirac semimetals. Here, we manipulate the band inversion responsible for the emergence of Dirac nodes by alloying Cd_3As_2 with topologically trivial Zn_3As_2 . We observe the expected topological phase transition around a Zn concentration of $x \sim 1$ while the carrier density monotonically decreases as x is increased. For larger x , the thermoelectric figure of merit exhibits comparably large values exceeding 0.3 at room temperature, due to the combined effects of a strong enhancement of the thermopower, an only moderate increase of the resistivity, and a suppression of the thermal conductivity. Complementary quantum-oscillation data and optical-conductivity measurements allow to infer that the enhanced thermoelectric performance is due to a flattening of the band structure in the higher- x region in $\text{Cd}_{3-x}\text{Zn}_x\text{As}_2$.

I. INTRODUCTION

Quantum transport of relativistic electrons in topological semimetals has been an issue of great interest in topological materials' science¹. In such materials, the quantum state of the Dirac or Weyl electrons is strongly coupled to the crystal symmetry, and hence the engineering of the electronic symmetry is a promising way to search for exotic quantum transport of such quasiparticles. In recent years more and more materials have been theoretically predicted and experimentally found to be a topological semimetal. Prototypical materials include $A_3\text{Bi}$ with $A = \text{Na}, \text{K}, \text{Rb}$ ²⁻⁴, BiO_2 and SbO_2 ⁵, and Cd_3As_2 ⁶⁻¹³.

Among them, Cd_3As_2 possesses a simple band structure with an electron charge carrier concentration of $\sim 10^{18} \text{ cm}^{-3}$. It has long been known for its large mobility of $\sim 10^4 \text{ cm}^2/\text{Vs}$ at room temperature¹⁴. Recently, an even higher value of almost $\sim 10^7 \text{ cm}^2/\text{Vs}$ was reported at low temperatures due to a linear band dispersion and strongly suppressed backscattering events of the charge carriers⁸. The nontrivial topology of this system, namely, an inversion of conduction and valence bands which are of different character, manifests in two Dirac nodes in the proximity of the Fermi energy E_F ⁶, which are protected by both time-reversal symmetry and rotational symmetry of the crystal lattice⁶. For example, it has been demonstrated that the breakdown of time-reversal symmetry via the application of a magnetic field creates a Weyl semimetallic state with negative magnetoresistance due to the chiral anomaly¹⁵⁻¹⁸, a hallmark of the underlying nontrivial physics.

Another way to control Dirac nodes in such systems is to manipulate the band inversion directly. It has been proposed that the chemical substitution of Cd with Zn changes the sign of band gap from negative (band inversion) to positive, resulting in the topological transition from a Dirac semimetal to a trivial insulator¹⁹⁻²². Indeed, in contrast to Cd_3As_2 , Zn_3As_2 is a topologically trivial semiconductor with a hole carrier concentration of $\sim 10^{17} \text{ cm}^{-3}$ and a much lower room-temperature mobility of only $\sim 10 \text{ cm}^2/\text{Vs}$ ¹⁴. Hence, a depletion of the charge carriers and a topological phase transition from the Dirac semimetal Cd_3As_2 to trivial Zn_3As_2 is expected when alloying these two systems. Indeed, Lu *et. al.*, found experimental indications of this transition in $\text{Cd}_{3-x}\text{Zn}_x\text{As}_2$ in magnetotransport measurements²² around $x \sim 1.1$ on the basis of an enhanced resistivity upon cooling as well as a thorough analysis of Shubnikov-de-Haas (SdH) oscillations. Recent studies on thin films of $\text{Cd}_{3-x}\text{Zn}_x\text{As}_2$ also support this scenario qualitatively²³⁻²⁵, although the topological phase transition takes place

already around $x \sim 0.6$ ²⁵. We note that a similar transition is proposed to occur in related $\text{Cd}_3\text{As}_{2-x}\text{P}_x$ on the basis of angle-resolved photoemission spectroscopy data²⁶.

Given the remarkably high mobility of the electron charge carriers, Cd_3As_2 is expected to bear potential for a good thermoelectric performance with possibly large power factors S_{xx}^2/ρ_{xx} ; S_{xx} and ρ_{xx} being the longitudinal thermopower and resistivity, respectively²⁷. Indeed, a recent study reported $S_{xx}^2/\rho_{xx} \sim 1.6 \times 10^{-3} \text{ W/K}^2/\text{m}$ along with a fairly small thermal conductivity $\kappa_{xx} \sim 5 \text{ W/K/m}$, yielding $ZT \sim 0.1$ at room temperature²⁸; ZT represents the figure of merit $ZT = S_{xx}^2 T / (\rho_{xx} \kappa_{xx})$ as a measure of the thermoelectric efficiency. This value further increases in presence of a magnetic field B , exceeding unity at $B = 7 \text{ T}$ and $T = 375 \text{ K}$ ²⁹ mainly due to field-induced suppression of κ_{xx} . Since these parameters also depend on the actual charge carrier concentration³⁰, it is promising to study the thermoelectric performance upon doping.

In this study, we have measured transport, thermoelectric properties, and the charge dynamics upon Zn doping in $\text{Cd}_{3-x}\text{Zn}_x\text{As}_2$ with $0 \leq x \leq 1.2$. With increasing x , the carrier density monotonically reduces and the Seebeck coefficient is largely enhanced, exceeding $300 \mu\text{V/K}$ at 300 K for $x = 1.2$. At low temperatures, we could confirm the reported metal-insulator transition with Zn doping²². At the same time, Zn doping suppresses the thermal conductivity while the resistivity above the metal-insulator transition temperature is enhanced only modestly due to the doping-induced disorder. Hence, the thermoelectric figure of merit is greatly enhanced, exceeding 0.3 at room temperature, i.e., more than three times the value reported for pure Cd_3As_2 . Complementary analyses of quantum oscillation and optical conductivity data suggest an x -dependent change in the band-structure dispersion in the higher doping region which promotes the enhancement of the figure of merit.

This paper is organized as follows: First, we will present electric and thermal transport data with enhanced ZT values. Then we will analyze magnetotransport and optical spectroscopy data which point toward the scenario of an x -dependent change of the band structure at E_F giving rise to the observed large room-temperature ZT values. We will finish with a discussion of our findings and conclude with a summary of the paper.

II. EXPERIMENTAL METHODS

Single-crystalline samples of Cd_3As_2 were grown by the Bridgmann technique, while polycrystalline samples of $\text{Cd}_{3-x}\text{Zn}_x\text{As}_2$ were synthesized by conventional melt-growth. In both cases, stoichiometric ratios of the constituent elements were mixed inside a glove box, transferred into quartz tubes, and eventually sealed while evacuated. In the Bridgman-method growth, the temperature of the upper (lower) heater was set to 900°C (600°C). The evacuated quartz tubes were kept for 12 h at 900°C and then lowered with a speed of 2 mm/h. After the quartz tubes had reached the lower heater, they were slowly cooled down to room temperature. Melt-grown batches were kept for 48 h at $800^\circ\text{C} - 950^\circ\text{C}$ depending on the composition and slowly cooled down to room temperature afterwards.

Resistivity and Hall effect were measured by a conventional five-probe method in a commercial system (PPMS, physical property measurement system, Quantum Design). The thermopower and thermal conductivity were measured in a home-built setup inserted into a PPMS while applying a temperature gradient by using a chip-heater attached on one side of the sample. The temperature gradient is monitored by employing commercial thermocouples. The reflectivity spectra at nearly normal incidence were measured between room temperature and 10 K in the energy region of $0.008 - 5$ eV. In the case of single-crystalline Cd_3As_2 , a sample surface with $[11\bar{2}]$ -orientation was polished. Then the spectra were measured with $[1\bar{1}0]$ light polarization. As for $\text{Cd}_{3-x}\text{Zn}_x\text{As}_2$, reflectivity spectra were measured with unpolarized light. A Fourier transform spectrometer and a grating-type monochromator equipped with a microscope were employed in the photon energy range $0.008 - 0.7$ eV and $0.5 - 5$ eV, respectively. Measurements in the energy range of $3 - 40$ eV were carried out at room temperature by using synchrotron radiation at UV-SOR, Institute for Molecular Science (Okazaki). For Kramers-Kronig transformations, we adopted suitable extrapolation procedures for energy ranges which were not accessible by the used experimental setups: below 0.008 eV the Hagen-Rubens-type (metal) or constant-reflectivity (insulator) extrapolation was used, respectively. Above 40 eV an ω^{-4} -type extrapolation was utilized.

III. RESULTS

Figure 1(a) shows the temperature dependence of the longitudinal resistivity ρ_{xx} for $\text{Cd}_{3-x}\text{Zn}_x\text{As}_2$. In the low-doped region ($0 \leq x \leq 0.6$), the resistivity decreases upon lowering temperature, i.e., the system behaves like a metal. The residual resistivity at 5 K is enhanced with increasing x as compared to our pure Cd_3As_2 sample except for $x = 0.2$. An upturn is clearly observed around ~ 120 K and ~ 170 K for $x = 1.0$ and $x = 1.2$, respectively, highlighting the metal-to-insulator transition in these higher-doped samples. The overall qualitative temperature dependence of the resistivities of $x = 1.0$ and 1.2 is similar. However, at very low temperatures there is a downturn in ρ_{xx} of the sample with $x = 1.0$, while the resistivity of the sample with $x = 1.2$ increases again after exhibiting a broad plateau between ~ 30 K and ~ 80 K. These features are clearly distinct from what is expected for a conventional insulator, the resistivity of which monotonically increases upon decreasing temperature.

Figure 1(b) summarizes the temperature dependence of the absolute value of the Hall coefficient R_H . For all x , R_H is nearly temperature independent and its sign is negative, indicating that the conduction in all examined samples is of electron type. Estimated carrier densities n_H at room temperature assuming a single carrier model are plotted against respective Zn concentrations in Fig. 1(c), together with n_Q estimated from quantum-oscillation data (see Fig. 3). As expected the absolute value of the carrier density monotonically decreases as a function of x from the order of a few times 10^{18}cm^{-3} for $x = 0$ down to $1.2 \times 10^{17}\text{cm}^{-3}$ for $x = 1.2$, reflecting the depletion of the electron-type carriers when going from n -type Cd_3As_2 to p -type Zn_3As_2 . However, the charge neutrality point, i.e., the Cd:Zn ratio where the sign change of R_H takes place, is not reached up to $x = 1.2$. We observe this crossover in slightly higher-doped samples around $x \sim 1.5$ (not shown). The metallic samples $x \leq 0.8$ investigated here exhibit mobilities of about $\sim 10^5 \text{ cm}^2/\text{V/s}$ at 2 K and $\sim 10^4 \text{ cm}^2/\text{V/s}$ at 300 K, respectively. We note that several properties, such as residual resistivity, charge carrier concentration etc. of this material are rather sample dependent as shown in Fig. 1(c); for $x = 0$ and 0.4 , there are exemplarily shown two charge carrier concentrations measured on two different samples, respectively. Such and even larger variations have been also reported for the parent material Cd_3As_2 , see, e.g., Ref. 8. This is possibly related to differences in the (Cd,Zn):As ratio. In Cd_3As_2 , ideally one fourth of the

Cd lattice sites are unoccupied and these vacancies seem to order in a chiral way along the c axis which may differ from sample to sample even if these samples were cut from the same initial batch³¹, cf. also the discussions in Refs. 7 and 8.

Thermoelectric and thermal-transport data are summarized in Figs. 2. The temperature dependence of the Seebeck coefficient S_{xx} is shown in Figs. 2(a) and (b) for $x \leq 0.6$ and $x \geq 0.8$, respectively. In the lightly-doped region $x \leq 0.8$, S_{xx} is negative and nearly proportional to temperature, which is often observed in conventional metals and semiconductors. By contrast, S_{xx} exhibits a nonmonotonic temperature dependence for larger x : below approximately 100 K and 170 K, S_{xx} deviates significantly from a temperature-linear behavior for $x = 1.0$ and 1.2, respectively. In particular, S_{xx} exhibits a sign change and becomes positive upon further cooling. Moreover, these temperatures nearly coincide with the upturn observed in resistivity data [see Fig. 1(a)].

The longitudinal thermal conductivity κ_{xx} is shown for selected x in Fig. 2(c). For all samples, κ_{xx} is almost temperature independent down to ~ 100 K but steeply increases towards lower temperatures possibly due to an enhancement of the phonon mean-free path. Interestingly, in the thermal conductivity there are no characteristic anomalies visible between 50 K and 200 K in clear contrast to resistivity (steep upturn) and thermopower data (clear slope change) even for $x = 1.2$, where these are most pronounced.

Absolute values of the Seebeck coefficient $|S_{xx}|$ at 300 K are replotted as a function of charge carrier concentration n_H in Fig. 2(d). The respective Zn concentrations x are given for each data point. Apparently, $|S_{xx}|$ increases monotonically with decreasing n_H : For our pure Cd_3As_2 sample, we find $|S_{xx}| = 44 \mu\text{V/K}$. For $x = 1.2$, $|S_{xx}|$ is enhanced by more than a factor of six, exceeding $300 \mu\text{V/K}$. This behavior is qualitatively consistent with the case of typical semiconductors or metals, where, according to Mott's formula, $|S_{xx}|$ is inversely proportional to E_F , which decreases here as indicated by the depletion of the electron carrier concentration with x , cf. Fig. 1(c). The dashed line in Fig. 2(d) indicates the expected charge-carrier-concentration dependence of $|S_{xx}|$ ($\propto n^{-1/3}$) in the semiclassical framework of Mott's formula with the assumption of a k -linear band dispersion. Apparently, this line fits well to the experimental data for $x \leq 0.6$ but clearly falls short for larger x .

The presented quantities allow us to calculate the thermoelectric figure of merit $ZT = S_{xx}^2 T / (\rho_{xx} \kappa_{xx})$, the room-temperature values of which are plotted against n_H in Fig. 2(e). As compared to pristine Cd_3As_2 ($ZT = 0.07$), ZT increases with x and exhibits a maximum

$ZT = 0.33$ for $x = 1.0$, a fairly large room-temperature value of the figure of merit. Here, we anticipate error bars of 30% because the values of ρ_{xx} , S_{xx} , and κ_{xx} are not precisely reproducible and depend on the sample used for the measurement, as already discussed above.

To obtain further insight into what mechanism might be responsible for the observed enhancement of the thermoelectric efficiency as represented by ZT , we investigated the impact of Zn doping on the electronic structure in $\text{Cd}_{3-x}\text{Zn}_x\text{As}_2$ by analyzing magnetoresistivity. Experimental data along with analyses of SdH oscillations are summarized in Fig. 3. The magnetoresistivity for $x = 0, 0.6$, and 0.8 are shown in Figs. 3(a), (b), and (c), respectively. For $x = 0$ and 0.6 , the resistivity is nearly proportional to the magnetic field and exhibits quantum oscillations, i.e. Shubunikov-de Haas (SdH). Such a B -linear magnetoresistivity is often observed in Dirac semimetals and is one characteristic feature of the highly mobile Dirac electrons¹. Similar SdH oscillations are also observed for $x = 0.8$ while the magnetoresistivity is rather quadratic in B in the low-field region.

Figure 3(d) contains the corresponding Landau level (LL) fan diagrams with the oscillation frequency $1/B$ plotted against the Landau index n_L . These were extracted according to the Lifshitz–Onsager quantization rule $B_F/B = n_L - \phi$ from the data shown in panels (a) – (c) after subtracting the background magnetoresistivity ρ_{BG} by approximating it with a polynomial. The resulting oscillation part ρ_{osc}/ρ_{BG} is exemplarily shown for $x = 0$ in the inset to Fig. 3(d). Then we assigned integer and half-integer indexes to the peak and valley positions in the magnetoresistivity data, respectively, as described in more detail, e.g., in Ref. 32. The linearity of the fan plot up to the quantum limit may be a consequence of small Zeeman splitting in this system. From the slope of the LL fan diagrams, the oscillation frequency B_F is estimated to be 58 T, 25 T, and 18 T for $x = 0, 0.6$, and 0.8 , respectively.

Figure 3(e) shows the temperature dependence of the background-corrected quantum oscillations ρ_{osc}/ρ_{BG} at selected magnetic fields. From the thermal damping of the oscillation amplitudes upon warming, the cyclotron mass is estimated to be $0.051m_0$, $0.033m_0$, and $0.029m_0$ in units of the bare electron mass m_0 for $x = 0, 0.6$, and 0.8 , respectively, by employing the Lifshitz-Kosevich formula³². We note that the Fermi velocity is nearly independent of the carrier density, suggesting that the band dispersion is close to k linear in this range of x . Table I summarizes these and additional parameters extracted from the SdH oscillations.

To obtain further insight into the electronic state, Fig. 4(a) shows the optical conductivity spectra at 10 K for $x = 0, 0.8$, and 1.2 . Spiky structures below 0.1 eV are ascribed to phonon excitations. As a common feature in all the three samples, the interband electron excitation from the valence to the conduction band manifests itself as a very slow increase of the optical conductivity as a function of the photon energy, which is often observed in gapless or small gap semimetals/semiconductors^{33–38}. Moreover, for each sample a small peak or kink is observed at about 0.2, 0.3, and 0.4 eV for $x = 0, 0.8$, and 1.2 , respectively, as indicated with black triangles in Fig. 4(a). We note that similar features are identified in the data taken at different temperatures, assuring that these kinks are an intrinsic feature. The kink is most remarkable in the case of $x = 0.8$. Such an absorption peak/kink was often observed and interpreted as the threshold of the interband transition^{33–35}. Apparently, this threshold energy is enhanced as x is increased. Taking into account that the carrier density is monotonically reduced upon increasing x , it is likely that the topological transition has occurred and a gap has opened in the case of the larger Zn concentration $x = 1.2$ as schematically illustrated in Fig. 4(c), in comparison with $x = 0$ shown in Fig. 4(b).

IV. DISCUSSION

Finally we will discuss the relevance of the observed electronic structure to the observed enhancement of the figure of merit exceeding 0.3 at room temperature. In the present case of a Dirac dispersion, the Fermi energy should be scaled to the Fermi wave number k_F which is proportional to $n^{1/3}$. According to Mott's formula, $|S_{xx}|$ is inversely proportional to E_F and, thus, is expected to scale with $n^{-1/3}$. As shown in Fig. 2(d) (dashed curve), the charge-carrier-concentration dependence of $|S_{xx}|$ is consistent with this semiclassical scaling for higher carrier densities, i.e., above $6 \times 10^{17} \text{ cm}^{-3}$ which corresponds to $x \lesssim 0.6$. However, when further increasing the Zn concentration, the coincidence becomes worse and eventually deviates significantly when the electron carriers become very diluted. In general, quantum oscillations are a highly sensitive probe of the electronic states in the vicinity of E_F while the Seebeck coefficient is strongly influenced or determined by the electronic states in an energy range of $\pm 4k_B T$ around E_F ³⁹. Hence, in the present case, the Seebeck coefficient may probe the energy dispersion in the energy range of $E_F/k_B \pm 1200 \text{ K}$. Thus, the significant discrepancy of the experimental Seebeck coefficients and the expectation in the semiclassical

model is likely to indicate that the band dispersion away from E_F is not linear in k any more in the heavily Zn-doped samples with $x > 0.6$ as sketched in Fig. 4(c). This strongly supports our initial working hypothesis that Zn doping is an efficient tool to tailor and finely tune the band structure in the Dirac semimetal Cd_3As_2 and should eventually trigger the topological phase transition.

The remaining question to be addressed is the origin of the thermally induced metal-insulator transition as indicated by the pronounced enhancement of ρ_{xx} below ~ 200 K for $x \geq 0.8$, which is also reflected in the nonmonotonous temperature dependence of the thermopower. Older literature reported a doping-induced structural transition in $\text{Cd}_{3-x}\text{Zn}_x\text{As}_2$ ²⁰. In order to look for a possible link between these two features, we performed temperature-dependent powder x-ray diffraction experiments on a sample with $x = 1.2$, but could not find any hint for a structural change upon cooling⁴⁰. Hence, the origin of this remarkable temperature-dependent change in resistivity and thermopower remains unclear and remains to be an interesting phenomenon to be elucidated for future studies.

V. SUMMARY

In summary, we demonstrate a topological transition in the Dirac semimetal Cd_3As_2 by engineering the band structure by replacing Cd with its lighter counterpart Zn with weaker spin-orbit interaction. Associated with this transition, the bands at the Fermi level are flattened and a strong enhancement of the thermopower is successfully induced. Moreover, the thermal conductivity is suppressed while the resistivity remains reasonably small, yielding a fairly large figure of merit $ZT = 0.33$ at $T = 300$ K. Our findings demonstrate that doping is an easy but highly efficient tool to control the topologically nontrivial band structure in Dirac semimetals and that such systems can be very promising starting points to look for an enhanced thermoelectric performance.

Acknowledgements

We thank D. Maryenko, T. Koretsune, R. Arita, T. Ideue and T. Liang for useful discussions and technical support. This work was partly supported by Grant-In-Aid for Science Research (Nos. 24224009, 15K05140, 16H00981, 18H01171, 18H04214, 16H06345) from the

MEXT, and by PRESTO(No. JPMJPR15R5) and CREST(No. JPMJCR16F1), JST (No. JP16H00924), Japan. JF and MK contributed equally to this work.

* corresponding author: fujioka@ims.tsukuba.ac.jp

† corresponding author: markus.kriener@riken.jp

- ¹ N. P. Armitage, E. J. Mele, and A. Vishwanath, *Rev. Mod. Phys.* **90**, 015001 (2018).
- ² Z. Wang, Y. Sun, X.-Q. Chen, C. Franchini, G. Xu, H. Weng, X. Dai, and Z. Fang, *Phys. Rev. B* **85**, 195320 (2012).
- ³ Z. K. Liu, B. Zhou, Y. Zhang, Z. J. Wang, H. M. Weng, D. Prabhakaran, S.-K. Mo, Z. X. Shen, Z. Fang, X. Dai, Z. Hussain, and Y. L. Chen, *Science* **343**, 864 (2014).
- ⁴ M. Neupane, S.-Y. Xu, R. Sankar, N. Alidoust, G. Bian, C. Liu, I. Belopolski, T.-R. Chang, H.-T. Jeng, H. Lin, A. Bansil, F. Chou, and M. Z. Hasan, *Nat. Commun.* **5**, 3786 (2014).
- ⁵ S. M. Young, S. Zaheer, J. C. Y. Teo, C. L. Kane, E. J. Mele, and A. M. Rappe, *Phys. Rev. Lett.* **108**, 140405 (2012).
- ⁶ Z. Wang, H. Weng, Q. Wu, X. Dai, and Z. Fang, *Phys. Rev. B* **88**, 125427 (2013).
- ⁷ M. N. Ali, Q. Gibson, S. Jeon, B. B. Zhou, A. Yazdani, and R. J. Cava, *Inorg. Chem.* **53**, 4062 (2014).
- ⁸ T. Liang, Q. Gibson, M. N. Ali, M. Liu, R. J. Cava, and N. P. Ong, *Nat. Mater.* **14**, 280 (2014).
- ⁹ Z. K. Liu, J. Jiang, B. Zhou, Z. J. Wang, Y. Zhang, H. M. Weng, D. Prabhakaran, S.-K. Mo, H. Peng, P. Dudin, T. Kim, M. Hoesch, Z. Fang, X. Dai, Z. X. Shen, D. L. Feng, Z. Hussain, and Y. L. Chen, *Nat. Mater.* **13**, 677 (2014).
- ¹⁰ S. Jeon, B. B. Zhou, A. Gyenis, B. E. Feldman, I. Kimchi, A. C. Potter, Q. D. Gibson, R. J. Cava, A. Vishwanath, and A. Yazdani, *Nat. Mater.* **13**, 851 (2014).
- ¹¹ M. Uchida, Y. Nakazawa, S. Nishihaya, K. Akiba, M. Kriener, Y. Kozuka, A. Miyake, Y. Taguchi, M. Tokunaga, N. Nagaosa, Y. Tokura, and M. Kawasaki, *Nat. Commun.* **8**, 2274 (2017).
- ¹² Y. Nakazawa, M. Uchida, S. Nishihaya, M. Kriener, Y. Kozuka, Y. Taguchi, and M. Kawasaki, *Sci. Rep.* **8**, 2244 (2018).
- ¹³ M. Uchida, T. Koretsune, S. Sato, M. Kriener, Y. Nakazawa, S. Nishihaya, Y. Taguchi, R. Arita, and M. Kawasaki, *Phys. Rev. B* **100**, 245148 (2019).

- ¹⁴ W. J. Turner, A. S. Fischler, and W. E. Reese, Phys. Rev. **121**, 759 (1961).
- ¹⁵ C.-Z. Li, L.-X. Wang, H. Liu, J. Wang, Z.-M. Liao, and D.-P. Yu, Nat. Commun. **6**, 10137 (2015).
- ¹⁶ J. Cao, S. Liang, C. Zhang, Y. Liu, J. Huang, Z. Jin, Z.-G. Chen, Z. Wang, Q. Wang, J. Zhao, S. Li, X. Dai, J. Zou, Z. Xia, L. Li, and F. Xiu, Nat. Commun. **6**, 7779 (2015).
- ¹⁷ H. Li, H. He, H.-Z. Lu, H. Zhang, H. Liu, R. Ma, Z. Fan, S.-Q. Shen, and J. Wang, Nat. Commun. **7**, 10301 (2016).
- ¹⁸ Z. Jia, C. Li, X. Li, J. Shi, Z. Liao, D. Yu, and X. Wu, Nat. Commun. **7**, 13013 (2016).
- ¹⁹ L. Żdanowicz and W. Żdanowicz, Phys. Solid State **6**, 227 (1964).
- ²⁰ W. Żdanowicz, K. Lukaszewicz, and W. Trzebiatowski, Bull. Acad. Pol. Sci. **12**, 169 (1964).
- ²¹ W. Żdanowicz and L. Żdanowicz, Annual Rev. Mater. Sci. **5**, 301 (1975).
- ²² H. Lu, X. Zhang, Y. Bian, and S. Jia, Sci. Rep. **7**, 3148 (2017).
- ²³ S. Nishihaya, M. Uchida, Y. Nakazawa, M. Kriener, Y. Kozuka, Y. Taguchi, and M. Kawasaki, Science Adv. **4**, eaar5668 (2018).
- ²⁴ S. Nishihaya, M. Uchida, Y. Nakazawa, K. Akiba, M. Kriener, Y. Kozuka, A. Miyake, Y. Taguchi, M. Tokunaga, and M. Kawasaki, Phys. Rev. B **97**, 245103 (2018).
- ²⁵ S. Nishihaya, M. Uchida, Y. Nakazawa, R. Kurihara, K. Akiba, M. Kriener, A. Miyake, Y. Taguchi, M. Tokunaga, and M. Kawasaki, Nat. Commun. **10**, 2564 (2019).
- ²⁶ S. Thirupathaiah, I. Morozov, Y. Kushnirenko, A. V. Fedorova, E. Haubold, T. K. Kim, G. Shipunov, A. Maksutova, O. Kataeva, S. Aswartham, B. Büchner, and S. V. Borisenko, Phys. Rev. B **98**, 085145 (2018).
- ²⁷ Y. Pei, X. Shi, A. LaLonde, H. Wang, L. Chen, and G. J. Snyder, Nature (London) **473**, 66 (2011).
- ²⁸ C. Zhang, T. Zhou, S. Liang, J. Cao, X. Yuan, Y. Liu, Y. Shen, Q. Wang, J. Zhao, Z. Yang, and F. Xiu, Chin. Phys. B **25**, 017202 (2016).
- ²⁹ H. Wang, X. Luo, W. Chen, N. Wang, B. Lei, F. Meng, C. Shang, L. Ma, T. Wu, X. Dai, Z. Wang, and X. Chen, Science Bull. **63**, 411 (2018).
- ³⁰ T. Zhou, C. Zhang, H. Zhang, F. Xiu, and Z. Yang, Inorg. Chem. Front. **3**, 1637 (2016).
- ³¹ T. Liang (private communication).
- ³² D. Maryenko, J. Falson, M. S. Bahramy, I. A. Dmitriev, Y. Kozuka, A. Tsukazaki, and M. Kawasaki, Phys. Rev. Lett. **115**, 197601 (2015).

- ³³ A. Akrap, M. Hakl, S. Tchoumakov, I. Crassee, J. Kuba, M. O. Goerbig, C. C. Homes, O. Caha, J. Novák, F. Teppe, W. Desrat, S. Koohpayeh, L. Wu, N. P. Armitage, A. Nateprov, E. Arushanov, Q. D. Gibson, R. J. Cava, D. van der Marel, B. A. Piot, C. Faugeras, G. Martinez, M. Potemski, and M. Orlita, *Phys. Rev. Lett.* **117**, 136401 (2016).
- ³⁴ D. Neubauer, J. P. Carbotte, A. A. Nateprov, A. Löhle, M. Dressel, and A. V. Pronin, *Phys. Rev. B* **93**, 121202(R) (2016).
- ³⁵ I. Crassee, E. Martino, C. C. Homes, O. Caha, J. Novák, P. Tückmantel, M. Hakl, A. Nateprov, E. Arushanov, Q. D. Gibson, R. J. Cava, S. M. Koohpayeh, K. E. Arpino, T. M. McQueen, M. Orlita, and A. Akrap, *Phys. Rev. Lett.* **97**, 125204 (2018).
- .
- ³⁶ G. S. Jenkins, C. Lane, B. Barbiellini, A. B. Sushkov, R. L. Carey, Fengguang Liu, J. W. Krizan, S. K. Kushwaha, Q. Gibson, Tay-Rong Chang, Horng-ay Jeng, Hsin Lin, R. J. Cava, A. Bansil and H. D. Drew, *Phys. Rev. B* **94**, 085121 (2016).
- ³⁷ J. Fujioka, R. Yamada, T. Okawa, and Y. Tokura, *Phys. Rev. B* **103**, L041109 (2021).
- ³⁸ R. Y. Chen, S. J. Zhang, J. A. Schneeloch, C. Zhang, Q. Li, G. D. Gu, and N. L. Wang, *Phys. Rev. B* **92**, 075107 (2015).
- ³⁹ H. Usui and K. Kuroki, *J. Appl. Phys.* **121**, 165101 (2017).
- ⁴⁰ See Supplemental Material for additional information on the crystal structure determined by the single crystalline X-ray diffraction.

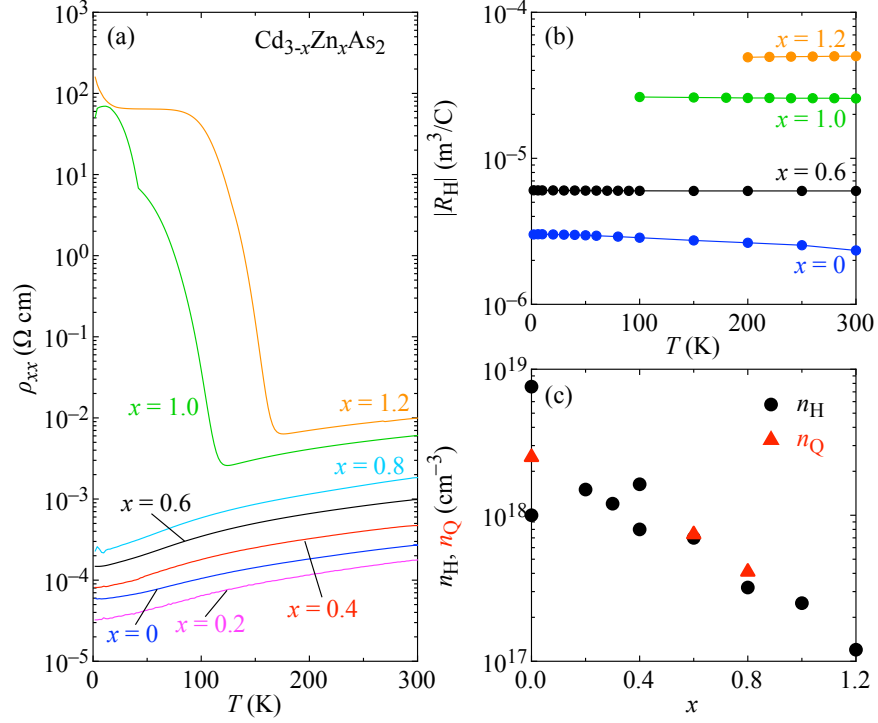


FIG. 1: Temperature dependence of (a) resistivity and (b) absolute value of the Hall coefficient $|R_H|$ for $\text{Cd}_{3-x}\text{Zn}_x\text{As}_2$. Here, R_H is negative for all x and the whole temperature range examined. (c) Carrier densities as a function of doping level x . Here, n_H (n_Q) denotes the carrier density derived from Hall coefficient data (quantum oscillations). n_Q is derived with assuming an isotropic Fermi surface.

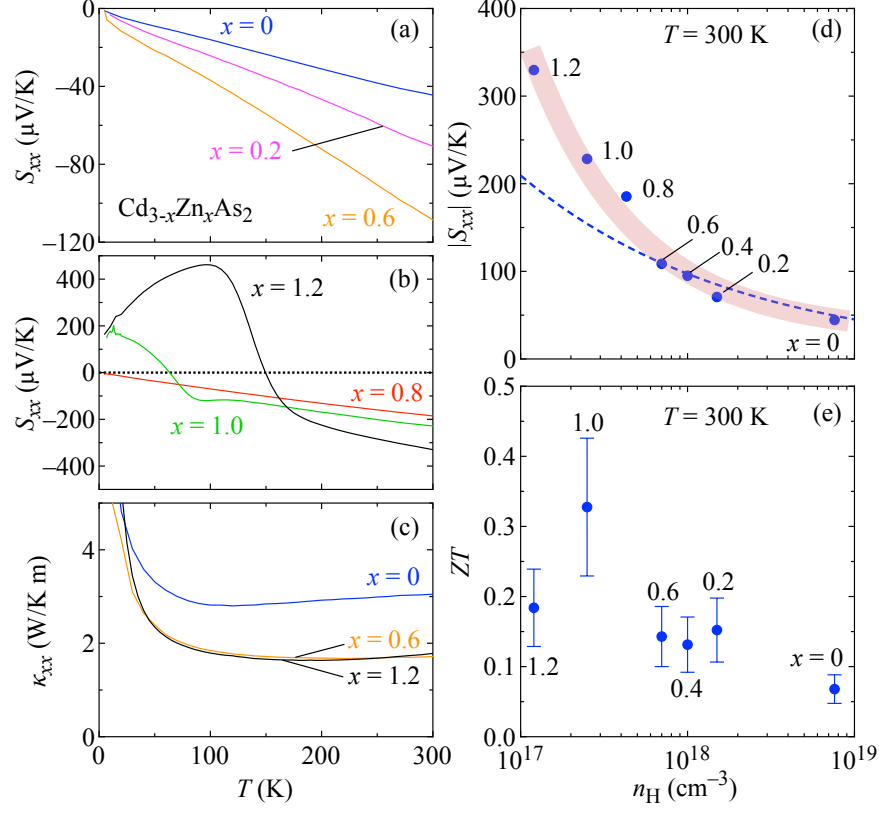


FIG. 2: Temperature dependence of the Seebeck coefficient (a) for $x = 0, 0.2$, and 0.6 and (b) for $x = 0.8, 1.0$, and 1.2 . (c) Thermal conductivity for $x = 0, 0.6$, and 1.2 . (d) Absolute value of the Seebeck coefficient $|S_{xx}|$ and (e) figure of merit ZT at 300 K plotted as function of the charge carrier concentration n_H for $0 \leq x \leq 1.2$. In (d), the dashed line indicates the semiclassical expectation $|S_{xx}| \propto n^{-1/3}$ assuming a k -linear band dispersion. The broad lightly-red shaded curve is merely a guide to the eyes.

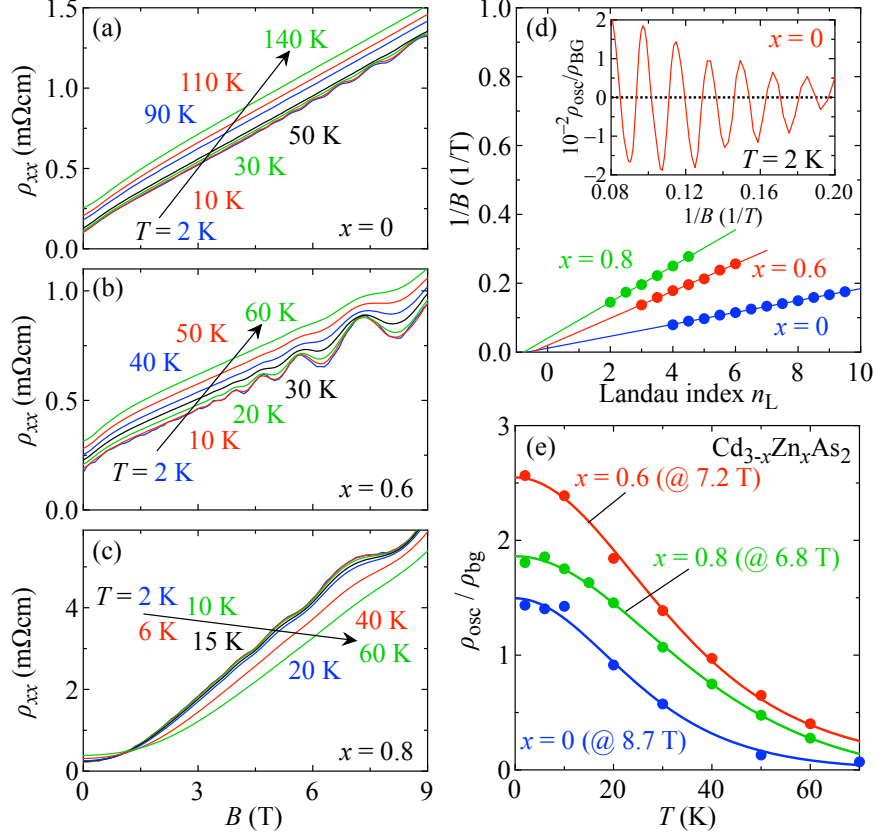


FIG. 3: Magnetoresistivity at various temperatures for (a) $x = 0$, (b) 0.6 and (c) 0.8, respectively. (d) Landau level fan diagram for $x = 0$ (blue), 0.6 (red), and 0.8 (green) at $T = 2$ K. In the inset, background-corrected quantum oscillations $\rho_{\text{osc}}/\rho_{\text{BG}}$ for $x = 0$ are shown as a function of $1/B$. (e) Temperature dependence of the amplitude of $\rho_{\text{osc}}/\rho_{\text{BG}}$ at selected field strengths as indicated in brackets next to the respective Zn concentrations [color code is the same as in panel (d)].

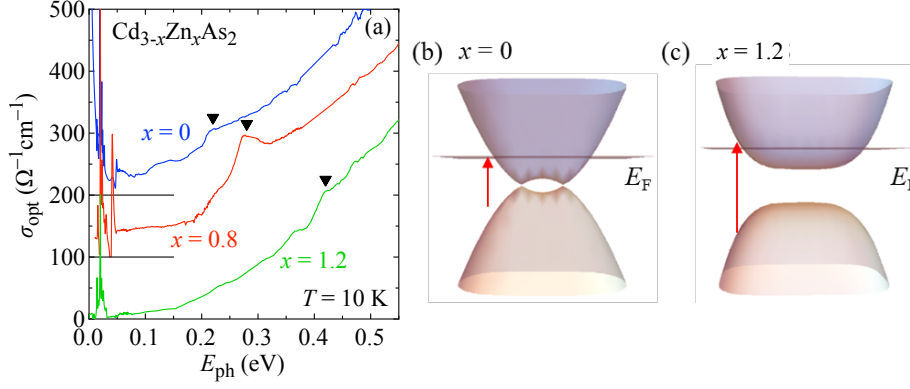


FIG. 4: (a) Optical conductivity spectra at 10 K for $x = 0$ (blue), 0.8 (red), and 1.2 (green). The spectra are shifted by $100\ \Omega^{-1}\text{cm}^{-1}$ with respect to each other for clarity. Solid black lines indicate the respective offsets. Triangles denote the threshold of interband transitions. The sharp peaks below 0.1 eV are attributed to optical phonons. Schematic illustration of the band dispersion for (b) $x = 0$ and (c) $x = 1.2$. The red arrow denotes the optical interband transition at the threshold energy marked with triangles in (a). The horizontal plane indicates the Fermi level E_F . See text for details.

TABLE I: Results of the analyses of the Shubnikov-de Haas (SdH) oscillations in magnetoresistivity data. Here, k_F denotes the Fermi wave vector, n_Q the electron-type charge carrier concentration as estimated from SdH oscillations, m_c/m_0 gives the cyclotron mass in units of the electron mass m_0 , v_F the Fermi velocity, T_D refers to the Dingle temperature, and τ_Q to the respective scattering time.

x	k_F (\AA^{-1})	n_Q (cm^{-3})	m_c/m_0	v_F (m/s)	T_D (K)	τ_Q (s)
0	0.042	2.5×10^{18}	0.051	9.4×10^5	12	1.0×10^{-13}
0.6	0.028	7.4×10^{17}	0.033	9.9×10^5	26	4.7×10^{-14}
0.8	0.023	4.1×10^{17}	0.029	9.3×10^5	10	1.2×10^{-13}